Interfaceless Exchange Bias in $CoFe_2O_4$ Nanocrystals

Beatriz Rivas-Murias,[1] Martín Testa-Anta,[2] Alexander S. Skorikov,[3] Miguel Comesaña-Hermo,[4] Sara Bals,[3] Verónica Salgueiriño[5,6]*

[1]CACTI, Universidade de Vigo, 36310 Vigo (Spain)

[2]Institut de Ciència de Materials de Barcelona (ICMAB-CSIC), Campus de la UAB, 08193 Bellaterra (Spain)

[3]Electron Microscopy for Materials Research (EMAT), University of Antwerp, Groenenborgerlaan 171, 2020 Antwerp (Belgium)

[4]Université Paris Cité, CNRS, ITODYS, Paris F-75013 Paris (France)

[5]Departamento de Física Aplicada, Universidade de Vigo, 36310 Vigo (Spain)

[6]CINBIO, Universidade de Vigo, 36310 Vigo (Spain)

Abstract

Oxidized cobalt ferrite nanocrystals with a modified distribution of the magnetic cations in their spinel structure give place to an unusual exchange-coupled system with a double reversal of the magnetization, exchange bias and increased coercivity, but without the presence of a clear physical interface that delimits two well-differentiated magnetic phases. More specifically, the partial oxidation of cobalt cations and the formation of Fe vacancies at the surface region entail the formation of a cobalt-rich mixed ferrite spinel which is strongly pinned by the ferrimagnetic background from the cobalt ferrite lattice. This particular configuration of exchange-biased magnetic behavior, involving two different magnetic phases but without the occurrence of a

crystallographically coherent interface, revolutionizes the established concept of the exchange bias phenomenology.

The exchange bias (EB) effect, also referred to as unidirectional or exchange anisotropy, describes a magnetic coupling observed in core-shell nanocrystals (NCs) or thin films, generally between an antiferromagnet (AFM) and a ferro- or ferrimagnet (FM and FiM, respectively) separated by a physical interface.[1] The EB effect with FM/FM, FiM/FiM, AFM/AFM or FM/spin glass exchange interactions has also been reported,[2–6] as well as more exotic systems stemming from interfacial spin configurations (that is, non-collinear or frustrated interface spins)[6–8] or even in magnetic NCs holding antiphase boundaries due to their strained crystalline structure.[9,10] Such coupling produces a horizontal shift in the hysteresis loop after cooling under an applied magnetic field, and is often accompanied by an increase in its coercive field (H_C), endorsing these systems with a huge relevance in many technological applications related to permanent magnets[11] or magnetic recording media.[12,13]

Given that EB is by definition an interfacial phenomenon dependent on a physical boundary between two well-differentiated magnetic components,[1,14] fine tuning of the dimensions, nature and overall quality of such interface is needed in order to control the magnetic coupling.[15,16] In this context, thin interfacial layers with FM or AFM properties generated at film-substrate interfaces, driven by a structural[17] or magnetic reconstruction,[18] as well as spin disorder,[19] can add new degrees of freedom for its engineering across heterointerfaces.

The origin of EB is known to lie on pinned uncompensated interfacial spins,[20] but a crucial influence of the inner (bulk) pinned uncompensated spins from the AFM component was recently demonstrated.[21] In fact, the interfacial spin distribution can be modified by the bulk AFM magnetic landscape, for instance via non-magnetic impurities or crystallographic defects, both of them conducive to AFM order dilution and the consequent AFM domain formation.[21,22] These

phenomena have been mostly investigated in AFM materials, but the underlying physical mechanism can be considered for their FiM counterparts.

Among the FiM candidates for the development of EB systems, combinations of different spinel ferrites stand out given their potential in spintronics.[23,24] These spinel-type oxides are prone to disorder and exchange processes on the cation sublattices, with the normal and inverse spinel as the two limiting cases under an ordered sublattice occupation. The disorder, if controlled, can perturb the ideal local coordination, for instance by inducing charge imbalances and ion vacancies, all of this having a huge impact on the heterostructure behavior. Consequently, the electrical and magnetic properties of these ferrites and, in general, of the transition metal oxide heterostructures,[25–27] can be modified when tailoring the interfacial and lattice characteristics through ionic motion.[28] Along these lines, a systematic tuning of the atomic distribution at the tetrahedral and octahedral sites of these spinel ferrites has opened new pathways for generating emergent phenomena in heterostructures due to ion migration.[29–31] Nevertheless, some control in the ion migration is required, to avoid the otherwise deleterious effects degrading the EB.[32]

Still, despite the important advances made in understanding the EB effect,[11,31] its analysis in single-phase objects lacking a core-shell or a layered structure, that is, lacking of a physical interface between two magnetic phases, has been reported scarcely.[10,11] Herein, we present a confined chemical treatment at the surface of single-crystallite $CoFe_2O_4$ NCs by which a change in the spinel crystalline structure is not appreciated but an ionic rearrangement in the subsurface and surface regions of the spherical NCs is induced. This situation offers a unique exchange coupling interaction within the same NC, without establishing a physical or coherent crystallographic interface. Yet, the magnetization reversal of the modified NCs is observed to occur in two steps and to come along with an increase in coercivity and an EB shift, suggesting the existence of a

strong exchange interaction between two magnetic components. The chemical changes registered, associated to the cation rearrangement in the spinel structure, help understand the magnetism displayed and underline the possibilities of this new chemical route for the engineering of EB-related functionalities for final device applications.

$CoFe_2O_4$ NCs with spherical shape and narrow size distribution (10.6 */1.3 nm average diameter (95.5%), log-normal fit) were synthesized by a seed-mediated growth (experimental details and Figure S1 in the Supporting Information (SI)). Figure 1a includes a TEM image of the NCs and Figure 1b shows its powder XRD pattern at room temperature, which is indexed to a cubic spinel structure (*Fd-3m* symmetry group) and allows to discard secondary phases. The cell parameter obtained from the Le Bail analysis is 0.8394 nm (see Table S1.1 in the SI), in good agreement with bulk cobalt ferrite (JCPDS card 22-1086).[33–35] Elementary analysis using ICP-OES indicates an average $Co_{0.95}Fe_{2.05}O_4$ stoichiometry (from now on referred to as $CoFe_2O_4$). A fraction of the same batch of these $CoFe_2O_4$ NCs was subsequently immersed and confined in a basic aqueous medium using a water-in-oil (W/O) reverse microemulsion, that is, stabilizing them by a nonionic surfactant (Igepal® CA-520) in water droplets in a hydrophobic continuous phase.[36] Besides the surfactant, these water droplets of very small volume exposed the NCs to a high pH, promoting an oxidation process at their surface.[36,37] This sample is hereafter labelled as $CoFe_2O_4$@Ox.
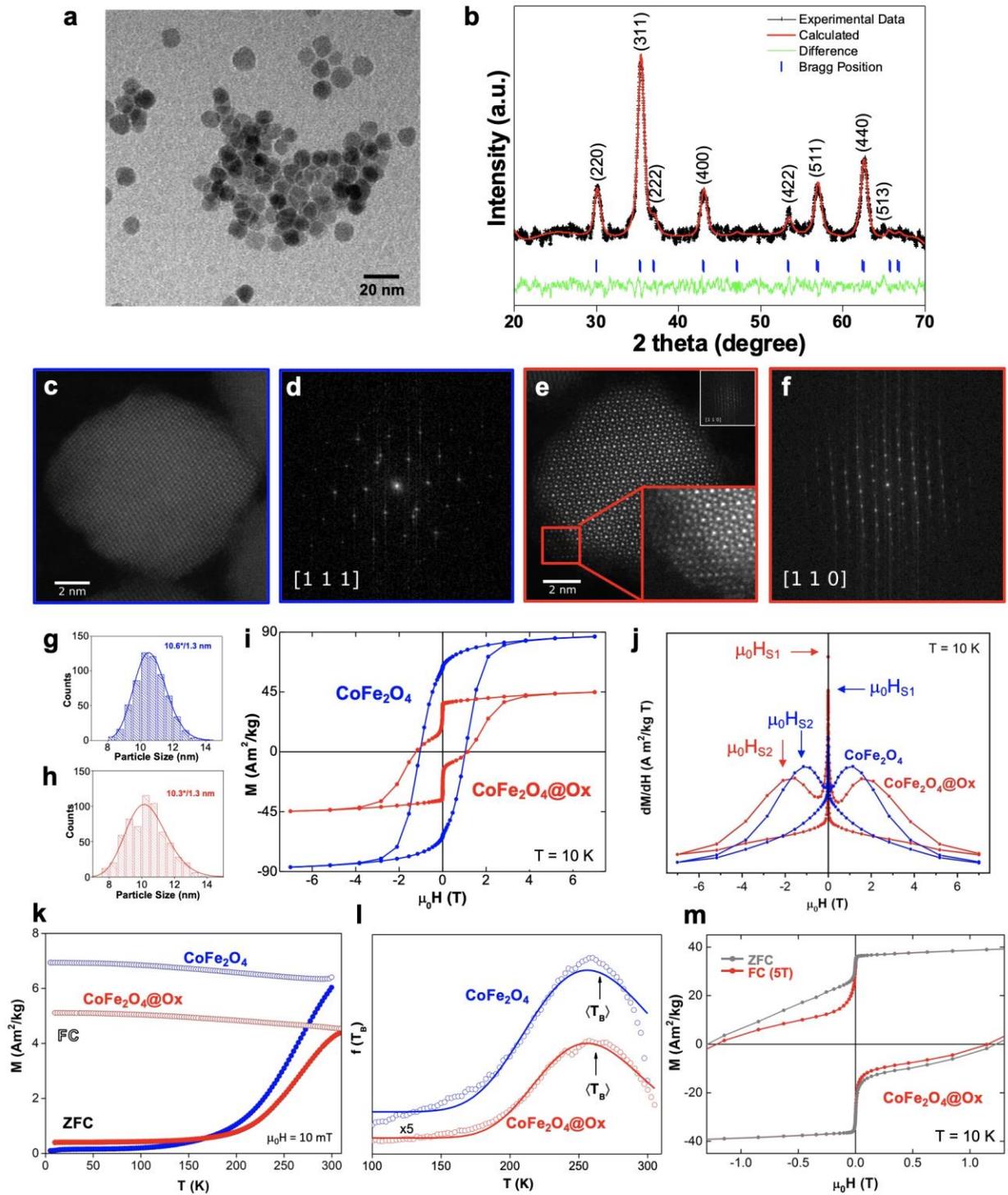
Figure 1. TEM image with general particle overview and X-ray diffraction pattern with Le Bail refinement of the CoFe₂O₄ NCs (a, b). HAADF-STEM images of representative CoFe₂O₄ (c) and CoFe₂O₄@Ox (e) NCs and their respective FFT images (d and f). Inset in (e): zoomed-in image of

the defect-free crystalline structure. Size histograms (fitted to log-normal functions) of $CoFe_2O_4$ (g) and $CoFe_2O_4$@Ox (h) NCs. Hysteresis loops measured at 10 K of $CoFe_2O_4$ (blue) and $CoFe_2O_4$@Ox (red) samples (i) and comparison of their derivatives, with μ_0H_{S1} and μ_0H_{S2} magnetic fields at which two events of magnetization switching occur (j). ZFC and FC curves measured at 10 mT (k) and distribution of energy barriers $f(T_B)$ calculated from the ZFC-FC curves and derivatives (l) of $CoFe_2O_4$ (blue dots) and $CoFe_2O_4$@Ox (red dots) samples. Hysteresis loops measured at 10 K of the $CoFe_2O_4$@Ox sample after ZFC (red) and FC at 5 T (gray) (m).

To shed light on the effect these conditions exert on the $CoFe_2O_4$ spinel structure, a high-angle annular dark-field scanning transmission electron microscopy (HAADF-STEM) study of the as-synthesized (Figure 1c and d and Figure S2a and c, $CoFe_2O_4$ sample) and the chemically-treated (Figure 1e and f and Figure S2b and d, $CoFe_2O_4$@Ox sample) NCs was performed. These images show no clear differences in the crystalline structure of these representative NCs, lacking in both cases the core-shell structure expected from a superficial oxidation. Indeed, the spinel crystalline lattice highlighted at these high resolution images has not defects, dislocations or twin boundaries up to the surface. The higher resolution image included in Figure 1e, obtained along the [110] zone axis, permits to appreciate distinct contrast associated to the positions of the atomic columns, offering an enlarged view of the defect-free spinel structure in the whole nanocrystal from the $CoFe_2O_4$@Ox sample. Interestingly, we can appreciate neither Moiré fringes nor grain or antiphase boundaries.[38] Moreover, the size histogram of the samples (fitted to log-normal function) does not show apparent modifications either (Figures 1g and 1h), and the analysis of atomic column positions in a 2D projection of a $CoFe_2O_4$@Ox NC shows the absence of systematic strain fields (Figure S3), thus excluding the presence of interfacial strain between two crystalline phases.

Yet, the magnetic behavior of the two $CoFe_2O_4$ and $CoFe_2O_4$@Ox samples points to an important change in the configuration of the magnetic cations in the spinel structure. Figure 1i includes the comparison of the magnetic properties displayed by the as-synthesized $CoFe_2O_4$ sample (blue curve) and by the $CoFe_2O_4$@Ox sample (red curve) at 10 K. The value of maximum magnetization registered for the $CoFe_2O_4$ sample is ~87 Am^2/kg when applying the maximum field (7 T), close to that of the bulk cobalt ferrite saturation magnetization ($M_{S(bulk)}$ ~90 Am^2/kg)[39] and similar to others values reported for NCs.[40,41] This is in agreement with the very good crystallinity of the NCs observed by HAADF-STEM and the stoichiometry registered. Anyhow, different effects related to a canted surface spin structure,[42] a gradient in the magnetic cations ratio moving outwards from the core to the surface,[43–45] or a cationic disorder in the crystalline structure at the surface can explain the slight difference. While this value of M_S when applying the maximum 7 T field drops to ~45 Am^2/kg for the $CoFe_2O_4$@Ox sample, the coercive field value increases (μ_0H_C = 1.06 T and μ_0H_C = 1.26 T for $CoFe_2O_4$ and $CoFe_2O_4$@Ox samples, respectively). In both cases, these high values of μ_0H_C are related to the high magnetostriction of $CoFe_2O_4$, due to the strong spin-orbit coupling from the Co^{2+} ions in the crystalline lattice.[43,46] In addition, the shape of the hysteresis loop has evolved after the chemical microemulsion-based treatment, with two reversals of magnetization (one of them much larger), seen as two inflection points (μ_0H_{S1} and μ_0H_{S2} magnetic fields) around 5 and 10 mT and 1.14 and 1.55 T when comparing the derivatives (dM/dH), shown in Figure 1j. The significantly larger reversal contribution at low field in the $CoFe_2O_4$@Ox sample clearly hints that a cationic modification took place. Similar contributions at low field were reported in samples of $CoFe_2O_4$ NCs synthesized by a co-precipitation method under alkaline conditions,[34,47,48] where phase segregation (due to Co_3O_4 and/or Fe_2O_3) or a phase with a reduced crystallinity was formed, but not detected in our samples in STEM. Figure 1k

displays the temperature dependent magnetization curves, measured under ZFC (zero-field cooled) and FC (field cooled) conditions and recorded applying a field of 10 mT. Whereas the mass magnetization value of the $CoFe_2O_4$@Ox has decreased notably in comparison to that of the initial sample (in line with the hysteresis loops), the shape of the ZFC and FC curves is very similar. Based on these ZFC-FC curves, it is possible to estimate the energy barrier distribution (in terms of the blocking temperature, T_B: $f(T_B) \propto (1/T) [d(M_{ZFC}-M_{FC})/dT]$,[49–51] fitted to a log-normal function in agreement with the size distribution, see Figures 1g, 1h and 1l). The average T_B values obtained are very similar, 265 and 262 K for $CoFe_2O_4$ and $CoFe_2O_4$@Ox samples, respectively, and comparable to other values of the literature.[40,52–54] This match in the blocking temperature reflects the very similar magnetically coherent volumes of FiM material in both samples,[55] despite the fact of observing two reversals of magnetization. Such finding is in line with the absence of an interface or any other crystalline defect in the crystalline structure, and the absence of byproducts (smaller nanoparticles and/or low anisotropy magnetic phases).

In order to further analyze the switching behavior in the $CoFe_2O_4$@Ox sample in terms of exchange-coupling properties, we measured the hysteresis loops in ZFC and FC conditions applying an external magnetic field of 5 T (Figure 1m). Though there is a decrease in coercivity, the FC hysteresis loop shows a negative field shift (μ_0H_E= -56.9 mT) associated to an EB effect. Such coupling, usually attributed to a FM/AFM interaction, is strong enough to produce a unidirectional anisotropy that causes the observed shift. The reduced coercivity registered for the $CoFe_2O_4$@Ox sample under FC conditions (compared to the ZFC loop) also unveils a reduction of the effective magnetic anisotropy, likely induced by the large cooling field. Similar trends have been reported in previous studies and ascribed to AFM order frustration.[56–58] In our case, this observation can be understood considering the presence of pinned uncompensated spins, which

align with the sufficiently large cooling field employed and induce frustration of the FiM exchange coupling. The presence of this hypothesized larger number of pinned uncompensated moments is supported experimentally by the large drop in the saturation magnetization but increased coercivity. Overall, these results point to a crucial influence of the synthetic conditions on the magnetic behavior of the $CoFe_2O_4$@Ox sample with respect to the as-synthesized one.

Aiming to corroborate the idea of the confined chemical effect in the micelles as the origin of the change in the magnetic behavior observed for the $CoFe_2O_4$@Ox sample, we performed an additional mapping of Fe and Co distribution and investigated their electronic configuration using electron energy loss spectroscopy (EELS). Figure 2a shows elemental mapping for $CoFe_2O_4$ and $CoFe_2O_4$@Ox samples, which indicates a similar increasing concentration of Co towards the surface of the nanocrystal in both cases. Although we cannot completely exclude an effect of electron beam irradiation, the results of different experimental techniques corroborate that $CoFe_2O_4$ or $MnFe_2O_4$ NCs synthesized via thermal decomposition typically have an increased content of Co or Mn at their surface, owing to the different decomposition temperature of the metallic precursors.[43–45,59] In this regard, the hysteresis loops of the initial sample show a very small reversal of magnetization at low field which can stem from the cobalt patches observed at the surface, and present in both native and oxidized samples. Anyway, the very large value of coercivity registered at low temperature can only be associated to the $Co_xFe_{3-x}O_4$ stoichiometry, even with increasing values of x as moving outwards. Additionally, EELS spectra of L edges for Fe and Co in $CoFe_2O_4$ and $CoFe_2O_4$@Ox samples (Figure 2b) reveal that: a) the L edge of Co in $CoFe_2O_4$@Ox is shifted by *ca*. +1.0 eV in comparison to $CoFe_2O_4$, indicating an increase in the oxidation state of Co, resulting from the chemical treatment,[60,61] and b) the ratio between the Fe L_3 and Co L_3 edges decreases from 2.95 in the $CoFe_2O_4$ sample to 2.59 in the $CoFe_2O_4$@Ox

sample, indicating an average decrease in the iron content. These experimental results point to a partial oxidation of cobalt cations and the formation of Fe vacancies in the spinel structure at the subsurface region, providing an explanation for the presence of pinned uncompensated moments associated to the changes in the magnetic behavior of the $CoFe_2O_4$@Ox sample and, particularly, to the EB effect.
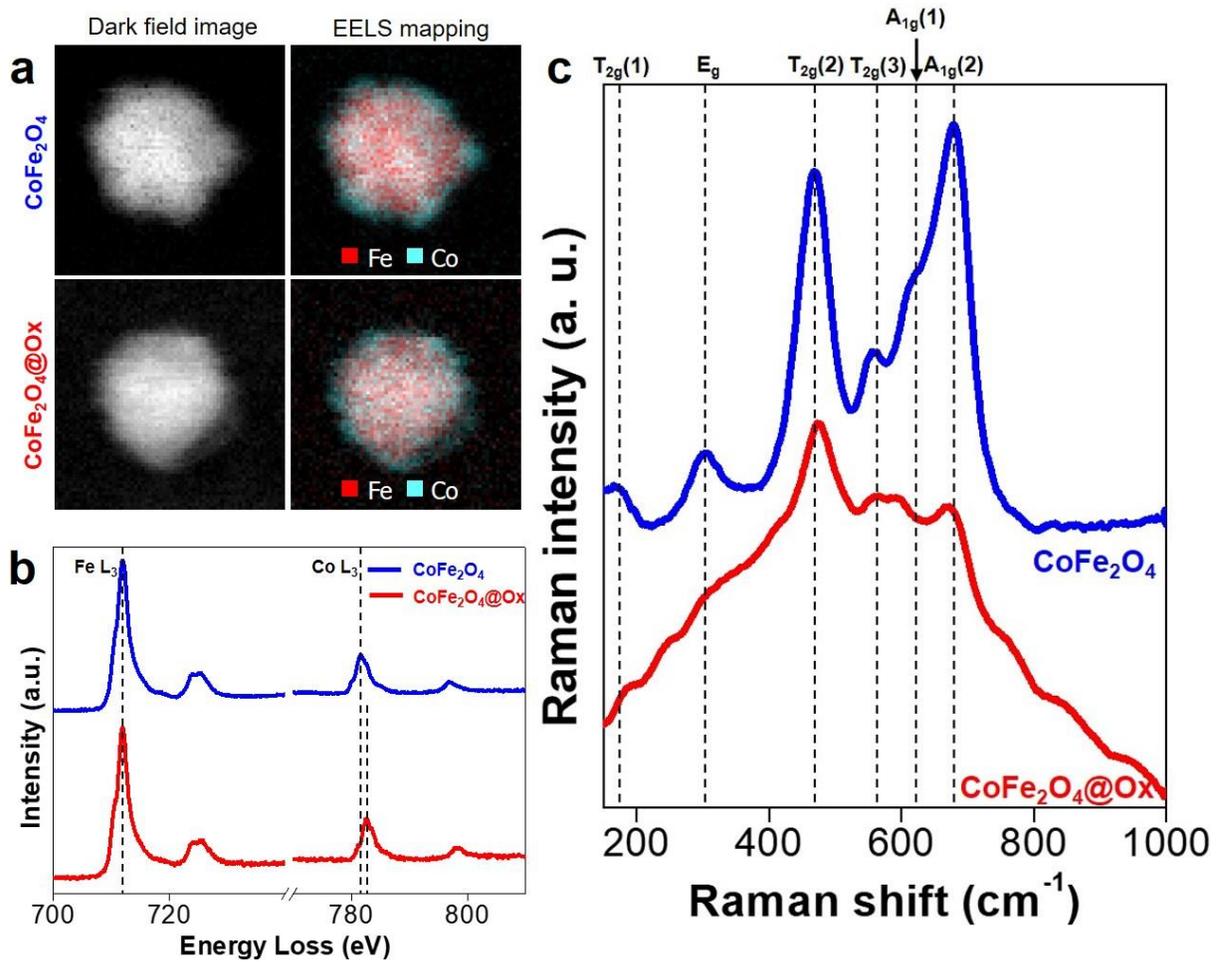

Figure 2. (a) Mapping of Fe and Co distribution in $CoFe_2O_4$ and $CoFe_2O_4$@Ox NCs based on EELS. (b) Comparison of EELS spectra for L edges of Fe and Co between $CoFe_2O_4$ and $CoFe_2O_4$@Ox samples. The dashed lines in the Co L_3 edge point out the shift of the edge position after oxidation. (c) Stokes-shifted Raman spectra registered using a 785 nm excitation wavelength from the $CoFe_2O_4$ (blue curve) and the $CoFe_2O_4$@Ox (red curve) samples.

To further support this relationship, we performed a Raman analysis of the as-synthesized $CoFe_2O_4$ and $CoFe_2O_4$@Ox samples in order to investigate the chemical/structural origin of the peculiar magnetic features observed.[62] This technique can register six Raman active modes from the spinel structure, namely $2A_{1g}$, E_g, and $3T_{2g}$, characteristic of spinels with two different types of cations occupying the octahedral or tetrahedral sites, such as $CoFe_2O_4$ (see Figure S4 in the SI).[63] In general, the ferrite A_{1g} modes appear above 600 cm^{-1} and are usually assigned to the motion of oxygen in the tetrahedral AO_4 group along the $\langle 111 \rangle$ direction, involving a symmetric stretching of the oxygen atoms with respect to the metal ion at the tetrahedral void (T),[64] as well as the deformation of the three octahedral sites (O) nearest to each oxygen.[65] Figure 2c includes the Raman spectra registered. In the as-synthesized sample (blue spectrum) the expected modes for the spinel lattice are observed,[66] with the most intense peak at 679 cm^{-1} ($A_{1g}(2)$) and a small shoulder at ~620 cm^{-1} ($A_{1g}(1)$), which stem from the presence of Fe^{3+} and Co^{2+} ions at the tetrahedral sites, respectively.[65,67] Note that the $A_{1g}(1))$ mode intensity is much lower than that of $A_{1g}(2)$, meaning that the primary contribution to the AO_4 vibrations originates from the Fe^{3+} ions. There is less consensus regarding the origin of the other low-frequency modes (E_g and T_{2g}), typically assigned to the tetrahedral unit in the Fe_3O_4 material,[64,68] or to the octahedral unit when considering mixed spinel ferrites such as $CoFe_2O_4$ or $ZnFe_2O_4$.[69,70] In the latter case, the E_g vibrational mode has been assigned to the symmetric bending of oxygen with respect to Fe in the octahedral BO_6 void[64] and is usually absent in nanocrystals.[71] The fact that this mode can be ascertained in our spectrum underlines once again the optimal crystallinity of the $CoFe_2O_4$ NCs. On the other hand, the $T_{2g}(2)$ mode has been reported to account solely for the Co^{2+} ions occupying the octahedral sites.[72] Hence, the higher intensity of the $T_{2g}(2)$ and the $A_{1g}(2)$ modes compared to

the $A_{1g}(1)$ mode confirms the predominant inverse spinel configuration anticipated for the cobalt ferrite.

The characteristic features of the spinel crystalline structure are still present in the $CoFe_2O_4$@Ox spectrum (red curve). However, the relative intensities of the A_{1g} and T_{2g} vibration modes have notably changed; being the $T_{2g}(2)$ mode (at ~470 cm^{-1}) the most prominent feature in the Raman spectrum. Interestingly, the vibrational modes $T_{2g}(3)$ and $A_{1g}(1)$ begin to merge into one broad band owing to the pronounced red-shift of the $A_{1g}(1)$ mode, now located at ~600 cm^{-1} (see also Figure S4). This shift is usually associated to structural distortions and/or the presence of a different set of cations at the tetrahedral/octahedral sites. Taking into account the absence of strain fields (Figure S3) and the *ca.* +1.0 eV shift observed in the Co L edge from the $CoFe_2O_4$@Ox sample (compared to $CoFe_2O_4$) (Figure 2b), the red-shift of the $A_{1g}(1)$ mode is consistent with the presence of Co^{3+} cations within the spinel structure, in addition to Fe^{3+} and Co^{2+}.[67] The resultant charge compensation of the crystalline structure may proceed via Fe vacancies[73] or a partial Fe^{3+}/Fe^{2+} reduction. While the presence of Fe^{3+} vacancies is supported by the decrease in the Fe/Co L_3 ratio registered, which indicates a reduced iron content in the $CoFe_2O_4$@Ox sample with respect to the pristine sample, the partial Fe^{3+}/Fe^{2+} reduction seems less probable, given the absence of observable changes in the L edge of the Fe spectrum in the EELS analysis. The fact that we have not registered the vacancies in the HAADF-STEM analysis suggests that their content must be rather small. Along these lines, the decrease in the $A_{1g}(2)$ mode intensity can be explained by this chemical and local modification promoted by the Fe^{3+} vacancies created. The oxidation of some of the Co^{2+} ions to Co^{3+} and the changes associated to the Fe^{3+} ions raise the question whether a non-stoichiometric $Co^{II}Co^{III}Fe^{III}$• O_4 spinel is formed at the subsurface region, but since the HAADF-STEM analysis reveals no evidence of two crystallographic phases at the core and the

surface shell, the as-formed mixed ferrite spinel must be highly disordered in terms of the metallic cation distribution. This disorder is also hinted by the presence of additional features in the Raman spectrum of the $CoFe_2O_4$@Ox sample, displaying new modes of low intensity at 420 and 760 cm^{-1}, for instance.

An additional experiment registering the evolution of the Raman spectra as a function of the incident laser power was also performed for the two $CoFe_2O_4$ and $CoFe_2O_4$@Ox systems (Figure S5). The Raman spectrum of the as-synthesized sample evolves into the same signature observed for $CoFe_2O_4$@Ox when treated under a laser power of 5.82 mW (Figure S5a), which can be associated to a partial oxidation of Co^{2+} cations reported above.[74] Furthermore, the very similar spectra recorded at 0.42 mW, after subjecting both samples to the highest laser power (21 mW) (Figure S5a and b), exhibit a remarked increase in the $T_{2g}(2)$ mode intensity compared to the $A_{1g}(2)$ mode, in agreement with a reduced iron content due to Fe^{3+} vacancy formation. The presence of these vacancies can be understood as a preliminary step prior to the transformation toward maghemite (γ-Fe_2O_3), and is also corroborated by the blue-shift of the $A_{1g}(2)$ mode to ~690 cm^{-1} (note that the A_{1g} mode characteristic from maghemite occurs at ~700 cm^{-1}).

Conclusively, to explain the coupling mechanism and the local magnetic configuration given the chemical changes registered by EELS and Raman spectroscopy and given the fact that there is no crystallographically coherent interface, we take the coercivity of the initial $CoFe_2O_4$ NCs as reference ($\mu_0H_C = 1.06$ T). With this large value into account, the fraction of $CoFe_2O_4$ phase at the outer shell of the as-synthesized NCs switches readily ($\mu_0H_{S1} = 5$ mT) (Figure 1j). However, for the $CoFe_2O_4$@Ox sample, while the magnetic phase at the subsurface region now switches with a value of $\mu_0H_{S1} = 10$ mT, the $CoFe_2O_4$ phase at the core follows an even larger switching field ($\mu_0H_{S2} = 1.55$ T). This can be explained considering the presence of unpinned uncompensated

moments in the cation disordered subsurface region of the $CoFe_2O_4$@Ox sample, which couple to the external field and rotate along with the FiM $CoFe_2O_4$ core, resulting in a coercivity enhancement.[21,22] On the other hand, the rather strong negative μ_0H_E field (-56.9 mT) indicates the presence of pinned uncompensated moments that strongly couple to the FiM lattice but do not rotate even at the maximum field (7 T). The presence of these pinned and unpinned magnetic moments can be understood as the outcome of competing interactions within the parental spinel structure, where the Co^{2+} oxidation has the Fe-O-Fe and Co-O-Fe superexchange interactions disrupted, leading to a highly frustrated subsurface region. This increased magnetic frustration, boosted by the assumed cation disorder, is reflected not only in the drop in the value of magnetization down to 45 Am^2/kg (which can be explained by the presence of low-spin Co^{3+} on octahedral sites[75]), but also in the low-anisotropy component detected during the reversal of the $CoFe_2O_4$@Ox sample. This fact hints that, besides inducing magnetic disorder, some short-range correlated spin disorder occurs. This situation, particularly in terms of the effects stemming from the presence of Co^{3+} and the iron vacancies, inducing a charge reorganization, with local modifications of the valence charge states and possible creation of defect gap states, can explain the changes not only in the magnetization, but also in the electronic, ionic and tunnel conductivities.[76] Such effects require a more in-depth investigation that falls out of the scope of the present study. Alternative scenarios in the attained cation distribution at the subsurface, such as a change from an inverse to a normal spinel configuration,[77,78] would lead to a magnetization enhancement and can be therefore discarded.

Summarizing, whereas the HAADF-STEM images show NCs with a uniform crystalline structure up to the surface and without the presence of defects or strain, both EELS and Raman spectroscopy, jointly with the magnetic properties, point to the presence of a pseudo core-shell structure with no

physical interface. Such unusual characteristics render the system particularly fascinating, pointing to a interfaceless exchange coupling between two different distributions of magnetic cations within the parent spinel structure.

Additional information

The Supporting Information is available free of charge on the ACS Publications website at DOI: XXXX. Experimental methods; supplementary Le Bail refinement data, HAADF-STEM data, strain analysis; supplementary magnetic data and supplementary Raman spectroscopy analysis.

Author information

Corresponding authors

*E-mail: vsalgue@uvigo.es

ORCID

Beatriz Rivas-Murias: 0000-0002-8048-5364

Martín Testa-Anta: 0000-0003-4437-2589

Alexander S. Skorikov: 0000-0001-8870-5344

Miguel Comesaña-Hermo: 0000-0001-8471-5510

Sara Bals: 0000-0002-4249-8017

Verónica Salgueiriño: 0000-0002-9396-468X

Notes

The authors declare no competing financial interest.

References

(1)   Nogués, J.; Schuller, I. K. Exchange Bias. *J. Magn. Magn. Mater.* **1999**, *192* (2), 203–232.

(2)   Schubert, C.; Hebler, B.; Schletter, H.; Liebig, A.; Daniel, M.; Abrudan, R.; Radu, F.; Albrecht, M. Interfacial Exchange Coupling in Fe-Tb/[Co/Pt] Heterostructures. *Phys. Rev. B* **2013**, *87*, 054415.

(3)   Hebler, B.; Reinhardt, P.; Katona, G. L.; Hellwig, O.; Albrecht, M. Double Exchange Bias in Ferrimagnetic Heterostructures. *Phys. Rev. B* **2017**, *95*, 104410.

(4)   Romer, S.; Marioni, M. A.; Thorwarth, N. R. J.; Corticelli, C. E.; Hug, H. J.; Oezer, S.; Parlinska-Wotjan, M.; Rohrmann, H. Temperature Dependence of Large Exchange-Bias in TbFe-Co/Pt. *Appl. Phys. Lett.* **2012**, *101*, 222404.

(5)   Borchers, J. A.; Carey, M. J.; Erwin, R. W.; Majkrzak, C. F.; Berkowitz, A. E. Spatially Modulated Antiferromagnetic Order in CoO/NiO Superlattices. *Phys. Rev. Lett.* **1993**, *70* (12), 1878–1881.

(6)   Ali, M.; Adie, P.; Marrows, C. H.; Greig, D.; Hickey, B. J.; Stamps, R. L. Exchange Bias Using a Spin Glass. *Nat. Mater.* **2007**, *6* (1), 70–75.

(7)   Testa-Anta, M.; Rivas-Murias, B.; Salgueiriño, V. Spin Frustration Drives Exchange Bias Sign Crossover in $CoFe_2O_4$–Cr_2O_3 Nanocomposites. *Adv. Funct. Mater.* **2019**, *29*, 1900030.

(8)   Zhang, J.; Yang, J.; Causer, G. L.; Shi, J.; Klose, F.; Huang, J.-K.; Tseng, A.; Wang, D.; Zu, X.; Qiao, L.; Pham, A.; Li, S. Realization of Exchange Bias Control with Manipulation of Interfacial Frustration in Magnetic Complex Oxide Heterostructures. *Phys. Rev. B* **2021**, *104* (17), 174444.

(9)   Levy, M.; Quarta, A.; Espinosa, A.; Figuerola, A.; Wilhelm, C.; García-Hernández, M.; Genovese, A.; Falqui, A.; Alloyeau, D.; Buonsanti, R.; Cozzoli, P. D.; García, M. A.; Gazeau, F.; Pellegrino, T. Correlating Magneto-Structural Properties to Hyperthermia Performance of Highly Monodisperse Iron Oxide Nanoparticles Prepared by a Seeded-Growth Route. *Chem. Mater.* **2011**, *23*, 4170–4180.

(10)   Wetterskog, E.; Tai, C.-W.; Grins, J.; Bergström, L.; Salazar-Alvarez, G. Anomalous

Magnetic Properties of Nanoparticles Arising from Defect Structures: Topotaxial Oxidation of $Fe_{1-X}O|Fe_{3-\Delta}O_4$ Core|Shell Nanocubes to Single-Phase Particles. *ACS Nano* **2017**, *7*, 7132–7144.

(11) Lottini, E.; López-Ortega, A.; Bertoni, G.; Turner, S.; Meledina, M.; Tendeloo, G. Van; De Julián Fernández, C.; Sangregorio, C. Strongly Exchange Coupled Core|Shell Nanoparticles with High Magnetic Anisotropy: A Strategy toward Rare-Earth-Free Permanent Magnets. *Chem. Mater.* **2016**, *28* (12), 4214–4222.

(12) Skumryev, V.; Stoyanov, S.; Zhang, Y.; Hadjipanayis, G.; Givord, D.; Nogués, J. Beating the Superparamagnetic Limit with Exchange Bias. *Nature* **2003**, *423* (6942), 850–853.

(13) Allibe, J.; Fusil, S.; Bouzehouane, K.; Daumont, C.; Sando, D.; Jacquet, E.; Deranlot, C.; Bibes, M.; Barthélémy, A. Room Temperature Electrical Manipulation of Giant Magnetoresistance in Spin Valves Exchange-Biased with BiFeO3. *Nano Lett.* **2012**, *12* (3), 1141–1145.

(14) López-Ortega, A.; Estrader, M.; Salazar-Alvarez, G.; Roca, A. G.; Nogués, J. Applications of Exchange Coupled Bi-Magnetic Hard/Soft and Soft/Hard Magnetic Core/Shell Nanoparticles. *Phys. Rep.* **2015**, *553*, 1–32.

(15) Liu, C.; Yu, C.; Jiang, H.; Shen, L.; Alexander, C.; Mankey, G. J. Effect of Interface Roughness on the Exchange Bias for NiFe/FeMn. *J. Appl. Phys.* **2000**, *87* (9), 6644–6646.

(16) Wang, J.; Sannomiya, T.; Shi, J.; Nakamura, Y. Influence of Interface Roughness on the Exchange Bias of Co/CoO Multilayers. *J. Appl. Phys.* **2013**, *113* (17), 17D707.

(17) Gilbert, D. A.; Olamit, J.; Dumas, R. K.; Kirby, B. J.; Grutter, A. J.; Maranville, B. B.; Arenholz, E.; Borchers, J. A.; Liu, K. Controllable Positive Exchange Bias via Redox-Driven Oxygen Migration. *Nat. Commun.* **2016**, *7*, 11050.

(18) Chen, A.; Wang, Q.; Fitzsimmons, M. R.; Enriquez, E.; Weigand, M.; Harrell, Z.; McFarland, B.; Lü, X.; Dowden, P.; MacManus-Driscoll, J. L.; Yarotski, D.; Jia, Q. Hidden Interface Driven Exchange Coupling in Oxide Heterostructures. *Adv. Mater.* **2017**, *29* (26), 1700672.

(19) Zhang, Q.; Liu, Z.; Ma, X. Magnetic Transition and the Associated Exchange Bias, Transport Properties in Mn $_{2.1}$ FeSn $_{0.9}$ Alloy. *J. Phys. D. Appl. Phys.* **2021**, *54* (50), 505001.

(20) Ohldag, H.; Scholl, A.; Nolting, F.; Arenholz, E.; Maat, S.; Young, A. T.; Carey, M.; Stöhr,

J. Correlation between Exchange Bias and Pinned Interfacial Spins. *Phys. Rev. Lett.* **2003**, *91* (1), 017203.

(21) Schuller, I. K.; Morales, R.; Batlle, X.; Nowak, U.; Güntherodt, G. Role of the Antiferromagnetic Bulk Spins in Exchange Bias. *J. Magn. Magn. Mater.* **2016**, *416*, 2–9.

(22) Wee, L.; Stamps, R. L.; Malkinski, L.; Celinski, Z. Rotatable Anisotropy and Mixed Interfaces: Exchange Bias in Fe / KNiF 3. *Phys. Rev. B* **2004**, *69* (13), 134426.

(23) Emori, S.; Yi, D.; Crossley, S.; Wisser, J. J.; Balakrishnan, P. P.; Khodadadi, B.; Shafer, P.; Klewe, C.; N'Diaye, A. T.; Urwin, B. T.; Mahalingam, K.; Howe, B. M.; Hwang, H. Y.; Arenholz, E.; Suzuki, Y. Ultralow Damping in Nanometer-Thick Epitaxial Spinel Ferrite Thin Films. *Nano Lett.* **2018**, *18* (7), 4273–4278.

(24) Li, P.; Xia, C.; Zhu, Z.; Wen, Y.; Zhang, Q.; Alshareef, H. N.; Zhang, X.-X. Ultrathin Epitaxial Ferromagnetic γ-Fe_2O_3 Layer as High Efficiency Spin Filtering Materials for Spintronics Device Based on Semiconductors. *Adv. Funct. Mater.* **2016**, *26*, 5679–5689.

(25) Sulpizio, J. A.; Ilani, S.; Irvin, P.; Levy, J. Nanoscale Phenomena in Oxide Heterostructures. *Annu. Rev. Mater. Res.* **2014**, *44* (1), 117–149.

(26) Goodenough, J. B. *Magnetism and the Chemical Bond*; John Wiley And Sons, 1963.

(27) Ndione, P. F.; Shi, Y.; Stevanovic, V.; Lany, S.; Zakutayev, A.; Parilla, P. A.; Perkins, J. D.; Berry, J. J.; Ginley, D. S.; Toney, M. F. Control of the Electrical Properties in Spinel Oxides by Manipulating the Cation Disorder. *Adv. Funct. Mater.* **2014**, *24* (5), 610–618.

(28) Maier, J. Pushing Nanoionics to the Limits: Charge Carrier Chemistry in Extremely Small Systems. *Chem. Mater.* **2014**, *26* (1), 348–360.

(29) Fontaiña-Troitiño, N.; Rivas-Murias, B.; Rodríguez-González, B.; Salgueiriño, V. Exchange Bias Effect in $CoO@Fe_3O_4$ Core-Shell Octahedron-Shaped Nanoparticles. *Chem. Mater.* **2014**, *26*, 5566–5575.

(30) Fontaiña-Troitiño, N.; Liébana-Viñas, S.; Rodríguez-González, B.; Li, Z.-A.; Spasova, M.; Farle, M.; Salgueiriño, V. Room-Temperature Ferromagnetism in Antiferromagnetic Cobalt Oxide Nanooctahedra. *Nano Lett.* **2014**, *14*, 640–647.

(31) López-Ortega, A.; Lottini, E.; Bertoni, G.; De Julián Fernández, C.; Sangregorio, C. Topotaxial Phase Transformation in Cobalt Doped Iron Oxide Core/Shell Hard Magnetic Nanoparticles. *Chem. Mater.* **2017**, *29* (3), 1279–1289.

(32) Lentijo-Mozo, S.; Deiana, D.; Sogne, E.; Casu, A.; Falqui, A. Unexpected Insights about Cation-Exchange on Metal Oxide Nanoparticles and Its Effect on Their Magnetic Behavior. *Chem. Mater.* **2018**, *30* (21), 8099–8112.

(33) Wohlfarth, E. P. *Ferromagnetic Materials : A Handbook on the Properties of Magnetically Ordered Substances. Volume 2 Volume 2*; North-Holland: Amsterdam [etc.], 1980.

(34) Pereira, C.; Pereira, A. M.; Fernandes, C.; Rocha, M.; Mendes, R.; Fernández-García, M. P.; Guedes, A.; Tavares, P. B.; Grenèche, J.-M.; Araújo, J. P.; Freire, C. Superparamagnetic MFe_2O_4 (M = Fe, Co, Mn) Nanoparticles: Tuning the Particle Size and Magnetic Properties through a Novel One-Step Coprecipitation Route. *Chem. Mater.* **2012**, *24*, 1496–1504.

(35) Deepak, F. L.; Bañobre-López, M.; Carbó-Argibay, E.; Cerqueira, M. F.; Piñeiro-Redondo, Y.; Rivas, J.; Thompson, C. M.; Kamali, S.; Rodríguez-Abreu, C.; Kovnir, K.; Kolenko, Y. V. A Systematic Study of the Structural and Magnetic Properties of Mn-, Co-, and Ni-Doped Colloidal Magnetite Nanoparticles. *J. Phys. Chem. C* **2015**, *119* (21), 11947–11957.

(36) Koole, R.; Van Schooneveld, M. M.; Hilhorst, J.; De Donegal, C. M.; 'T Hart, D. C.; Van Blaaderen, A.; Vanmaekelbergh, D.; Meijerink, A. On the Incorporation Mechanism of Hydrophobic Quantum Dots in Silica Spheres by a Reverse Microemulsion Method. *Chem. Mater.* **2008**, *20* (7), 2503–2512.

(37) Lee, D. C.; Mikulec, F. V.; Pelaez, J. M.; Koo, B.; Korgel, B. A. Synthesis and Magnetic Properties of Silica-Coated FePt Nanocrystals. *J. Phys. Chem. B* **2006**, *110*, 11160–11166.

(38) Fontaiña-Troitiño, N.; Ramos-Docampo, M. A.; Testa-Anta, M.; Rodríguez-González, B.; Bañobre-López, M.; Bocher, L.; McKenna, K. P.; Salgueiriño, V. Antiphase Boundaries in Truncated Octahedron-Shaped Zn-Doped Magnetite Nanocrystals. *J. Mater. Chem. C* **2018**, *6*, 12800–12807.

(39) Cullity, B. D.; Graham, C. D. *Introduction to Magnetic Materials*; John Wiley And Sons, 2008.

(40) Peddis, D.; Cannas, C.; Musinu, A.; Ardu, A.; Orruì, F.; Fiorani, D.; Laureti, S.; Rinaldi, D.; Muscas, G.; Concas, G.; Piccaluga, G. Beyond the Effect of Particle Size: Influence of $CoFe_2O_4$ Nanoparticle Arrangements on Magnetic Properties. *Chem. Mater.* **2013**, *25* (10), 2005–2013.

(41) Gomide, G.; Cabreira Gomes, R.; Gomes Viana, M.; Cortez Campos, A. F.; Aquino, R.;

López-Ortega, A.; Perzynski, R.; Depeyrot, J. Nanoparticle Size Distribution and Surface Effects on the Thermal Dependence of Magnetic Anisotropy. *J. Phys. Chem. C* **2022**, *126*, 1581–1589.

(42) Peddis, D. Magnetic Properties of Spinel Ferrite Nanoparticles: Influence of the Magnetic Structure. *Magn. Nanoparticle Assem.* **2014**, *7*, 978–981.

(43) Sathya, A.; Guardia, P.; Brescia, R.; Silvestri, N.; Pugliese, G.; Nitti, S.; Manna, L.; Pellegrino, T. $Co_xFe_{3-X}O4$ Nanocubes for Theranostic Applications: Effect of Cobalt Content and Particle Size. *Chem. Mater.* **2016**, *28* (6), 1769–1780.

(44) Ijiri, Y.; Krycka, K. L.; Hunt-Isaak, I.; Pan, H.; Hsieh, J.; Borchers, J. A.; Rhyne, J. J.; Oberdick, S. D.; Abdelgawad, A.; Majetich, S. A. Correlated Spin Canting in Ordered Core-Shell $Fe_3O_4/Mn_xFe_{3-X}O_4$ Nanoparticle Assemblies. *Phys. Rev. B* **2019**, *99*, 094421.

(45) Yan, Z.; FitzGerald, S.; Crawford, T. M.; Mefford, O. T. Manganese and Cobalt Substituted Ferrite Nanoparticles Synthesized via a Seed-Mediated Drip Method. *JPhys Mater.* **2021**, *4*, 034013.

(46) Zhou, B.; Zhang, Y. W.; Yu, Y. J.; Liao, C. S.; Yan, C. H.; Chen, L. Y.; Wang, S. Y. Correlation between Structure and Intervalence Charge-Transfer Transitions in Nanocrystalline $CoFe_{2-X}M_xO_4$ (M=Mn, Al, Sc) Thin Films. *Phys. Rev. B* **2003**, *68*, 024426.

(47) Zeb, F.; Qureshi, A. R.; Nadeem, K.; Mumtaz, M.; Krenn, H. Surface Effects in Uncoated and Amorphous SiO_2 Coated Cobalt Ferrite Nanoparticles. *J. Non. Cryst. Solids* **2016**, *435*, 69–75.

(48) Gyergyek, S.; Makovec, D.; Kodre, A.; Arčon, I.; Jagodič, M.; Drofenik, M. Influence of Synthesis Method on Structural and Magnetic Properties of Cobalt Ferrite Nanoparticles. *J. Nanoparticle Res.* **2010**, *12* (4), 1263–1273.

(49) Micha, J. S.; Dieny, B.; Régnard, J. R.; Jacquot, J. F.; Sort, J. Estimation of the Co Nanoparticles Size by Magnetic Measurements in Co/SiO_2 Discontinuous Multilayers. *J. Magn. Magn. Mater.* **2004**, *272–276*, e967–e968.

(50) Mamiya, H.; Ohnuma, M.; Nakatani, I.; Furubayashim, T. Extraction of Blocking Temperature Distribution from Zero-Field-Cooled and Field-Cooled Magnetization Curves. *IEEE Trans. Magn.* **2005**, *41* (10), 3394–3396.

(51) Bruvera, I. J.; Mendoza Zélis, P.; Pilar Calatayud, M.; Goya, G. F.; Sánchez, F. H.

Determination of the Blocking Temperature of Magnetic Nanoparticles: The Good, the Bad, and the Ugly. *J. Appl. Phys.* **2015**, *118* (18).

(52)   López-Ortega, A.; Lottini, E.; Fernández, C. D. J.; Sangregorio, C. Exploring the Magnetic Properties of Cobalt-Ferrite Nanoparticles for the Development of a Rare-Earth-Free Permanent Magnet. *Chem. Mater.* **2015**, *27* (11), 4048–4056.

(53)   Gu, Z.; Xiang, X.; Fan, G.; Li, F. Facile Synthesis and Characterization of Cobalt Ferrite Nanocrystals via a Simple Reduction−Oxidation Route. *J. Phys. Chem. C* **2008**, *112*, 18459–18466.

(54)   Torres, T. E.; Roca, A. G.; Morales, M. P.; Ibarra, A.; Marquina, C.; Ibarra, M. R.; Goya, G. F. Magnetic Properties and Energy Absorption of $CoFe_2O_4$ Nanoparticles for Magnetic Hyperthermia. *J. Phys. Conf. Ser.* **2010**, *200*, 072101.

(55)   Knobel, M.; Nunes, W. C.; Socolovsky, L. M.; De Biasi, E.; Vargas, J. M.; Denardin, J. C. Superparamagnetism and Other Magnetic Features in Granular Materials: A Review on Ideal and Real Systems. *J. Nanosci. Nanotechnol.* **2008**, *8*, 2836–2857.

(56)   Leighton, C.; Nogués, J.; Jönsson-Åkerman, B. J.; Schuller, I. K. Coercivity Enhancement in Exchange Biased Systems Driven by Interfacial Magnetic Frustration. *Phys. Rev. Lett.* **2000**, *84* (15), 3466–3469.

(57)   Perzanowski, M.; Zarzycki, A.; Gregor-Pawlowski, J.; Marszalek, M. Magnetization Reversal Mechanism in Exchange-Biased Spring-like Thin-Film Composite. *ACS Appl. Mater. Interfaces* **2020**, *12* (35), 39926–39934.

(58)   Rostamnejadi, A.; Venkatesan, M.; Kameli, P.; Salamati, H.; Coey, J. M. D. Cooling-Field Dependence of Exchange Bias Effect in $La_{0.45}Sr_{0.55}MnO_3$ Nanoparticles. *J. Appl. Phys.* **2014**, *116* (4), 043913.

(59)   Hoene, J. Von; Charles, R. G.; Hickam, W. M. Thermal Decomposition of Metal Acetylacetonates: Mass Spectrometer Studies. *J. Phys. Chem.* **1958**, *62*, 1098–1101.

(60)   Wang, Z. L.; Bentley, J.; Evans, N. D. Valence State Mapping of Cobalt and Manganese Using Near-Edge Fine Structures. *Micron* **2000**, *31*, 355–362.

(61)   Bazin, D.; Kovács, I.; Guczi, L.; Parent, P.; Laffon, C.; De Groot, F.; Ducreux, O.; Lynch, J. Genesis of Co/SiO_2 Catalysts: XAS Study at the Cobalt LIII,II Absorption Edges. *J. Catal.* **2000**, *189* (2), 456–462.

(62) Testa-Anta, M.; Ramos-Docampo, M. A. M. A.; Comesaña-Hermo, M.; Rivas-Murias, B.; Salgueiriño, V. Raman Spectroscopy to Unravel the Magnetic Properties of Iron Oxide Nanocrystals for Bio-Related Applications. *Nanoscale Adv.* **2019**, *1*, 2086–2103.

(63) White, W. B.; DeAngelis, B. A. Interpretation of the Vibrational Spectra of Spinels. *Spectrochim. Acta Part A Mol. Spectrosc.* **1967**, *23*, 985–995.

(64) Shebanova, O. N.; Lazor, P. Raman Spectroscopic Study of Magnetite ($FeFe_2O_4$): A New Assignment for the Vibrational Spectrum. *J. Solid State Chem.* **2003**, *174*, 424–430.

(65) Laguna-Bercero, M. A.; Sanjuán, M. L.; Merino, R. I. Raman Spectroscopic Study of Cation Disorder in Poly- and Single Crystals of the Nickel Aluminate Spinel. *J. Phys. Condens. Matter* **2007**, *19*, 186217.

(66) Chandramohan, P.; Srinivasan, M. P.; Velmurugan, S.; Narasimhan, S. V. Cation Distribution and Particle Size Effect on Raman Spectrum of $CoFe_2O_4$. *J. Solid State Chem.* **2011**, *184*, 89–96.

(67) Bahlawane, N.; Tchoua Ngamou, P. H.; Vannier, V.; Kottke, T.; Heberle, J.; Kohse-Höinghaus, K. Tailoring the Properties and the Reactivity of the Spinel Cobalt Oxide. *Phys. Chem. Chem. Phys.* **2009**, *11*, 9224–9232.

(68) Verble, J. L. Temperature-Dependent Light-Scattering Studies of the Verwey Transition and Electronic Disorder in Magnetite. *Phys. Rev. B* **1974**, *9*, 5236–5248.

(69) Liao, Y. Y.; Li, Y. W.; Hu, Z. G.; Chu, J. H. Temperature Dependent Phonon Raman Scattering of Highly A-Axis Oriented $CoFe_2O_4$ Inverse Spinel Ferromagnetic Films Grown by Pulsed Laser Deposition. *Appl. Phys. Lett.* **2012**, *100* (7), 071905.

(70) Wang, Z.; Schiferl, D.; Zhao, Y.; O'Neill, H. S. C. High Pressure Raman Spectroscopy of Spinel-Type Ferrite $ZnFe_2O_4$. *J. Phys. Chem. Solids* **2003**, *64* (12), 2517–2523.

(71) Singh, J. P.; Srivastava, R. C.; Agrawal, H. M.; Kumar, R. Micro-Raman Investigation of Nanosized Zinc Ferrite Effect of Crystallite Size and Fluence of Irradiation. *J. Raman Spectrosc.* **2011**, *42*, 1510–1517.

(72) Shemer, G.; Tirosh, E.; Livneh, T.; Markovich, G. Tuning a Colloidal Synthesis to Control Co^{2+} Doping in Ferrite Nanocrystals. *J. Phys. Chem. C* **2007**, *111* (39), 14334–14338.

(73) Pratt, A.; Lari, L.; Hovorka, O.; Shah, A.; Woffinden, C.; Tear, S. P.; Binns, C.; Kröger, R. Enhanced Oxidation of Nanoparticles through Strain-Mediated Ionic Transport. *Nat. Mater.*

2014, *13*, 26–30.

(74) Rivas-Murias, B.; Salgueiriño, V. Thermodynamic CoO–Co_3O_4 Crossover Using Raman Spectroscopy in Magnetic Octahedron-Shaped Nanocrystals. *J. Raman Spectrosc.* **2017**, *48*, 837–841.

(75) Eskandari, F.; Porter, S. B.; Venkatesan, M.; Kameli, P.; Rode, K.; Coey, J. M. D. Magnetization and Anisotropy of Cobalt Ferrite Thin Films. *Phys. Rev. Mater.* **2017**, *1* (7), 074413.

(76) Sharma, K.; Calmels, L.; Li, D.; Barbier, A.; Arras, R. Influence of the Cation Distribution, Atomic Substitution, and Atomic Vacancies on the Physical Properties of $CoFe_2O_4$ and $NiFe_2O_4$ Spinel Ferrites. *Phys. Rev. Mater.* **2022**, *6* (12), 124402.

(77) Rivas-Murias, B.; Testa-Anta, M.; Torruella, P.; Estradé, S.; Peiró, F.; Rodríguez-González, B.; Comesaña-Hermo, M.; Salgueiriño, V. Structural and Magnetic Implications of Transition Metal Migration within Octahedral Core-Shell Nanocrystals. *Chem. Mater.* **2020**, *32* (24), 10435–10446.

(78) Ferreiro-Vila, E.; Iglesias, L.; Lucas Del Pozo, I.; Varela-Dominguez, N.; Bui, C. T.; Rivas-Murias, B.; Vila-Fungueiriño, J. M.; Jimenez-Cavero, P.; Magen, C.; Morellon, L.; Pardo, V.; Rivadulla, F. Apparent Auxetic to Non-Auxetic Crossover Driven by Co^{2+} Redistribution in $CoFe_2O_4$ Thin Films. *APL Mater.* **2019**, *7*, 031109.

For Table of Contents Only